Materials Advances

ROYAL SOCIETY OF CHEMISTRY

PAPER

View Article Online
View Journal | View Issue

Cite this: *Mater. Adv.*, 2024, 5, 5080

Multifunctional MgAl LDH/Zn-MOF S-scheme heterojunction: efficient hydrogen production, methyl red removal, and CO_2 adsorption†

Ihsan Maseeh,‡[a] Farheen Anwar,‡[a] Sadia Aroob,[a] Tariq Javed,[b] Ismat Bibi,[a] Afaf Almasoudi,[c] Ahmad Raheel,[d] Muhammad Arshad Javid,[e] Sónia A. C. Carabineiro[f] and Muhammad Babar Taj*[a]

Metal–organic frameworks (MOFs) and layered double hydroxides (LDHs) are undoubtedly promising and valuable materials for developing advanced catalysts to achieve efficient hydrogen evolution. The unique structures, environmentally friendly nature, and high redox activities of these materials make them ideal for catalytic applications. In this study, a delicately constructed S-scheme heterojunction photocatalyst, denoted as MgAl LDH/Zn-MOF, was designed and synthesized through the *in situ* nucleation of Zn-MOF nanostructure on MgAl LDH nanosheets, based on their excellent electronic properties and opposite surface potential. The MgAl LDH/Zn-MOF photocatalyst exhibited enhanced photocatalytic hydrogen evolution activity (129 mmol g^{-1}) compared to Zn-MOF and MgAl LDH alone. This was mainly due to the formation of the MgAl LDH/Zn-MOF S-scheme heterojunction, which effectively accelerated the recombination of several electrons (from the conduction band of Zn-MOF) and holes (from the valence band of MgAl LDH), thus preventing the recombination of other electrons (from the conduction band of MgAl LDH) and holes (from the valence band of Zn-MOF), which is a critical requirement for efficient hydrogen evolution. Further, the MgAl LDH/Zn-MOF has a high potential for methyl red removal (97% following the intraparticle diffusion model with a maximum R^2 value of 0.996). The CO_2 adsorption isotherms of the MgAl LDH/Zn-MOF revealed a gravimetric CO_2 uptake capacity of 129.7 mg g^{-1} (at 298 K and 40 bar) and stable cyclic adsorption performance. These findings demonstrate the potential of MOFs and LDHs for developing advanced catalysts for efficient hydrogen evolution and highlight the importance of heterojunction design.

Received 12th January 2024,
Accepted 29th April 2024

DOI: 10.1039/d4ma00038b

rsc.li/materials-advances

1. Introduction

As our world continues to grow and develop, more people strive for a better quality of life.[1] This is a positive trend, but unfortunately, it has led to a significant increase in energy consumption. This overconsumption can potentially lead to a devastating energy crisis, which could have far-reaching consequences for our planet.[1] Along with this issue, we face several other environmental challenges, such as pollution, ecological destruction, increased greenhouse gas emissions, deforestation, and waste production. Our dependence on fossil fuels worsens these challenges, and this is a significant obstacle we must overcome to secure a sustainable future.[2] To address these issues, we must focus on developing clean and sustainable energy sources with the necessary adsorption capacity, selectivity, and regeneration capacity. That can reduce our dependence on fossil fuels and mitigate their negative environmental impact. It is a challenging task, that we must take on in order to build a brighter future for ourselves and generations to come.[3] Sunlight is the most significant and abundant energy source, whether directly or indirectly used. Nevertheless, the conversion and utilization of solar energy have not yet reached optimal levels. However, researchers have found a promising solution to this challenge – the light-induced water-splitting process. It involves splitting water molecules into hydrogen and oxygen with the help of sunlight, resulting in the production of hydrogen. This gas is

[a] *Institute of Chemistry, The Islamia University of Bahawalpur, Bahawalpur 63100, Pakistan. E-mail: dr.taj@iub.edu.pk*
[b] *Department of Chemistry, University of Sahiwal, Sahiwal 57000, Pakistan*
[c] *Chemistry Department, Faculty of Science, King Abdulaziz University, P.O. Box 42734, Jeddah, Saudi Arabia*
[d] *Department of Chemistry, Quaid-e-Azam University, Islamabad 44000, Pakistan*
[e] *Institute of Physics, The Islamia University Bahawalpur, Bahawalpur 63100, Pakistan*
[f] *LAQV-REQUIMTE, Department of Chemistry, NOVA School of Science and Technology, Universidade NOVA de Lisboa, 2829-516 Caparica, Portugal*

† Electronic supplementary information (ESI) available. See DOI: https://doi.org/10.1039/d4ma00038b

‡ Both authors have equal contributions, so they are considered first authors.

known for its high calorific value, environmental sustainability, and exceptional conversion efficiency. It is a clean and efficient energy source that holds immense potential to tackle the environmental and energy-related issues we face today.[4] Hydrogen has been identified as a feasible replacement for fossil fuels in electricity generation and transportation. The transition to a "hydrogen economy" requires innovative techniques for producing H_2, with photocatalytic water splitting and alcohol photo reforming using sunlight being the most promising methods.

Currently, various types of semiconductors are being investigated, such as zinc oxide (ZnO), titanium dioxide (TiO_2), cadmium sulfide (CdS), graphitic carbon nitride (g-C_3N_4), and copper oxide (CuO). Such materials can help us create better and more efficient ways to use sunlight to generate energy.[5] Other examples are the layered double hydroxides (LDHs). These are inorganic compounds with distinct two-dimensional layered structures that are attracting significant research interest due to cost-effective and facile preparation, well-designed structure, biocompatibility, and their ability to accommodate various guest species, such as organic and inorganic materials, nanoparticles, functional and polymers, thus being versatile for various applications.[6] These materials are typically designed using divalent and trivalent metal cations, although LDHs with monovalent and tetravalent cations are also reported. The general representation of an LDH is $[M_{1-x}^{2+}\ M_x^{3+}\ (OH)_2]^{x+}\ [A^{n-}]_{x/n}$, where M^{2+} represents divalent metal cations, like Cu^{2+}, Mg^{2+}, Ni^{2+}, Zn^{2+}, *etc.* M^{3+} refers to trivalent metal cations, like Al^{3+}, Fe^{3+}, Ga^{3+}, Mn^{3+}, *etc.* A^{n-} is an inorganic or organic anion that neutralizes the charge, such as SO_4^{2-}, Cl^-, NO_3^{1-}, *etc.* LDHs are cost-effective, abundant, and safe to use.[7] They are an exceptional class of two-dimensional clay materials uniquely suited for various applications,[8] such as energy storage, drug delivery, and photocatalysis, which uses sunlight to create chemical reactions.[9] LDHs exhibit high stability and a basic surface, which is of utmost importance in adsorption, making them incredibly promising materials for CO_2 adsorption.[10] However, LDHs have some limitations, such as poor crystalline structure and low electrical conductivity. The aggregation of irreversible exfoliated nanosheets in LDH unequivocally hinders the migration of photo-excited electrons and holes, leading to the undeniable suppression of photocatalytic reactions.[11,12] Different routes can be taken to improve LDHs performance by changing their structure and combining them with other materials. The formation of heterojunctions with other semiconductors is the most promising strategy for overcoming the shortcomings of the LDH photocatalyst in terms of charge separation and transfer efficiency.[13]

Metal–organic frameworks (MOFs) are highly porous materials with potential applications in catalysis, sensors, drug delivery, gas separation, and storage.[14] They are formed by arranging organic ligands and metal atomic cluster structures.[15] Different synthesis methods have been developed for MOFs, including ultrasonic synthesis and micro-emulsion technology.[15] Polycarboxylate organic ligands are effective building blocks.[16] In addition, MOFs are a type of coordination polymers with a crystal structure that offers potential porosity. This research field has rapidly developed in the past two decades.[17] MOFs can immobilize active functional materials and manufacture highly controllable nanostructures as carriers, providing new materials for energy applications.[18] A new photocatalyst, MgAl LDH/Zn-MOF, successfully designed and synthesized, is reported in this work. This material is a unique combination of Zn-based terephthalate frameworks with LDH (MgAl LDH), with excellent performance in photocatalytic hydrogen evolution due to its fast electron transfer. Moreover, it is also efficient in removing methyl red dye from water and CO_2 from a gas stream.

2. Material and methods

2.1. Materials

The adsorbents used in this study were prepared from high-purity chemicals. The precursors used for the synthesis of the adsorbents included magnesium nitrate ($Mg(NO_3)_2{\cdot}6H_2O$, 99% purity, Sigma Aldrich), aluminum nitrate ($Al(NO_3)_2{\cdot}9H_2O$, 99% purity, Sigma Aldrich), sodium hydroxide (NaOH, 98% purity, Sigma Aldrich), zinc nitrate ($Zn(NO_3)_2{\cdot}6H_2O$, 99% purity, Sigma Aldrich), and benzene-1,4-dicarboxylic acid ($C_8H_6O_4$, Sigma Aldrich). The dye used for adsorption was methyl red ($C_{15}H_{15}N_3O_2$, Sigma Aldrich). All chemicals were of high purity and were used without further treatment. The salt solutions were prepared using deionized water.

2.2. Synthesis of MgAl LDH

The synthesis of MgAl LDH (molar ratio 2 : 1) was performed by co-precipitation. Firstly, a 20 mmol solution of $Mg(NO_3)_2{\cdot}6H_2O$ and a 10 mmol solution of $Al(NO_3)_2{\cdot}9H_2O$ were prepared in separate beakers using 40 ml of deionized water each. In a separate beaker, 10 mmol of benzene-1,4-dicarboxylic acid (BDC) was dissolved in 70 ml of deionized water, and then 10 mmol of sodium hydroxide was added to the solution. The aqueous solutions of $Mg(NO_3)_2{\cdot}6H_2O$ and $Al(NO_3)_2{\cdot}9H_2O$ were slowly added dropwise to the benzene-1,4-dicarboxylic acid (BDC) solution under continuous stirring for 18 h. The pH of the solution was maintained at 10 by adding NaOH solution dropwise. The resulting white precipitate (BDC intercalated MgAl LDHs) was filtered and washed with deionized water to remove impurities. The precipitate was dried in a vacuum desiccator at room temperature.

2.3. Synthesis of MgAl LDH supported Zn-MOF nanocomposite

To obtain the MgAl-LDH/Zn-MOF nanocomposite (1 : 3), 3 g of MgAl LDH was dispersed in 50 ml of dimethylformamide. Then, a 8.99 mmol of $Zn(NO_3)_2{\cdot}6H_2O$ solution was prepared and added to the above solution. The mixture obtained was refluxed at 120 °C for 1 hour. This led to the creation of highly dispersed Zn-MOFs nanostructure through *in situ* nucleation and growth on MgAl LDH nanosheets. The blue-colored solution was then filtered, washed, and dried at room temperature in a vacuum desiccator. Zn-MOF was also prepared using

BDC[19] according to the reported method for comparative study of H_2 evolution.

2.4. Characterization

The synthesized samples were subjected to various characterization techniques to determine their structural, surface, and morphological properties. The techniques used include X-ray diffraction (XRD), scanning electron microscopy (SEM), UV-vis spectroscopy, fluorescence, Fourier transform infrared spectroscopy (FTIR), N_2 adsorption at 77 K and zeta potential (PZC). The crystalline structure and size of the adsorbents were characterized by powder XRD on a Bruker D8 Advance instrument, using Cu-Kα radiation with a wavelength of 1.541 Å. The vibrational frequencies of the prepared composites were determined using FTIR spectroscopy (Tensor 27 FTIR) in the range of 400 to 4000 cm^{-1}. The synthesis of MgAl LDH and MgAl-LDH/Zn-MOF was confirmed using a Cecil 7500 UV-vis spectrophotometer in the 200 to 800 nm range. The surface and morphological features of the composites were analyzed using SEM (MIRA-III TESCON). The pore size and specific surface area of MgAl-LDH/Zn-MOF were calculated by using surface area analyzer Gemini 2375, Shimadzu. To test the stability and surface charge of MgAl-LDH/Zn-MOF, a Zetasizer equipment (Nano-ZS, Malvern Instruments, UK) was used. Impedance spectroscopy (EIS) using electrochemical techniques was conducted by applying a 10 mV amplitude within a frequency range of 1 MHz to 1.0 Hz while keeping the potential constant at 200 mV (*vs.* Ag/AgCl). The working electrolyte used in the analysis was 0.1 M sodium sulfate dissolved in water. The electronic band structures were analyzed using ultraviolet photoemission spectroscopy (UPS) on a AXIS-Nova, Kratos Analytical Ltd; monochromatic (He I = 21.2 eV, Ag $3d_{5/2}$ < 100 meV). The high-pressure CO_2 adsorption performance was analyzed on an IsoSORP adsorption analyzer (TA instruments, New Castle, DE, USA).

2.5. Hydrogen production method

Experiments were conducted with precision to produce hydrogen through photocatalysis using a Pyrex reactor that was capable of being degassed and sampled. (The procedure used was similar to the one reported in the literature.[20,21]) The process involved the addition of 10 mg of catalytic material, 20 mg of Eosin Y (EY), and 20 ml (10% v/v) of triethanolamine (TEOA) into the reactor. Before exposing the solution to visible light, the excess gas was removed through vacuuming. The amount of hydrogen evolved was then analyzed using a gas chromatograph (Tianmei GC7900, with N_2 as the carrier) at different time intervals, using gas headspace samples (0.5 ml) injected into the gas chromatograph. The H_2 produced was quantified against an internal calibration curve. The rate of gas (H_2) evolution was measured in units of mmol g^{-1} and mmol g^{-1} h^{-1} to enable confident comparison between MgAl LDH, Zn-MOF, and MgAl LDH/Zn-MOF photocatalysts under identical conditions. The experiment was repeated at least three times for each sample to ensure accuracy beyond doubt. The external quantum efficiency (EQE) under identical photocatalytic reaction conditions, was calculated using the following eqn (1).

$$\mathrm{EQE} = \left(R_{H_2} \times 2 \times c \times h/I \times \lambda \times A\right) \times L \times 100 \quad (1)$$

where R_{H_2} is the rate of H_2 produced (mol s^{-1}), c is the speed of light (3.8×10^8 m s^{-1}), h is the Plank's constant (6.62×10^{-34} J s^{-1}), I is the light intensity (5.95 W cm^{-2} = J s^{-1} cm^{-2}), λ is the wavelength of incident light, A is the illuminated area of reactor (cm^2), and L is the Avogadro's constant (6.022×10^{23} mol^{-1}). Based on the H_2 production rate and the area of the reactor directly exposed to the sun (approximately 10 cm^2), the EQE was calculated to be 8.25%.

2.6. Methyl red adsorption studies

Studying dye adsorption under room temperature and atmospheric pressure is of significant interest.[22–24] A series of adsorption experiments were conducted in dark conditions to evaluate the effectiveness of the prepared adsorbents for removing methyl red (MR) dye. In each experiment, 25 mg of the prepared adsorbent was added to 25 ml of 5×10^{-5} M MR dye solution, and the mixture was stirred at 298 K for different reaction times. At 20 min intervals, a small sample of the mixture was removed for UV-visible analysis.

The adsorbent was separated from the mixture by centrifugation, and the remaining solution was analyzed using an ultraviolet-visible (UV-vis) spectrophotometer (Cecil 7500) to determine the concentration of MR dye at equilibrium (C_e) at 410 nm. After the adsorption reaction, the adsorbent was washed, filtered, and dried in an oven at 343 K.

The removal efficiency (R) and adsorption capacity (q) of the prepared adsorbents for MR dye can be calculated using the following eqn (2) and (3):[25]

$$R = \frac{C_o - C_e}{C_e} \times 100 \quad (2)$$

$$q = (C_o - C_e) \times \frac{V}{M} \quad (3)$$

where C_0 represents the initial concentration of MR in milligrams per liter, V is the volume of the dye solution in liters, M is the mass of the adsorbent used in grams, and R represents the removal efficiency expressed as a percentage. The adsorption capacity (q) is expressed as the amount of MR dye adsorbed per unit weight of the adsorbent (mg g^{-1}).

To examine the rate at which adsorption occurs, we analyzed experimental data using different models, such as pseudo-first-order kinetics, pseudo-second-order kinetics, liquid-film diffusion model, and intra-particle diffusion model. We also applied various isothermal models to the data, including the Langmuir, Freundlich, and Temkin models, to gain insight into the mechanism of dye removal. Additionally, we calculated the changes in Gibbs free energy (ΔG_o, kJ mol^{-1}), entropy (ΔS_o, kJ mol^{-1} K^{-1}), and enthalpy (ΔH_o, kJ mol^{-1}). (see ESI,† Section S1).

2.7. CO_2 adsorption performance

Experiment was conducted to study the adsorption of CO_2 using a previously reported procedure.[26] The experiment involved degassing 0.5 g of adsorbent at 383 K under high vacuum for 4 h. The sample mass and volume were subsequently determined using a buoyancy test with He at 295 K. The CO_2 adsorption–desorption isotherm of the MgAl LDH/Zn-MOF composite was then measured by dosing CO_2 from a high vacuum to 40 bar, followed by a high vacuum with an equilibrium point every 10 bar. The equilibrium for each step was maintained until the deviation of mass was less than 0.1 mg per 10 min. The results of this experiment provided valuable insight into the adsorption behavior of CO_2 and its potential applications in various industries.

3. Results and discussion

3.1. PXRD analysis

The phase structure and crystallinity of the synthesized nanocomposite were analyzed using XRD. Fig. 1(a) shows the MgAl LDH and MgAl-LDH/Zn-MOF nanocomposite diffractograms. The diffractogram of Zn-MOF (Fig. S2a, ESI†) shows 2θ values at 8.20, 10.52, and 13.28, which are assigned to the lattice planes of (200), (220), and (400), respectively, in agreement with the literature.[27–29] The presence of BDC between the layer of LDH is confirmed by the 2θ shift of the characteristic peak (003)[30] from 11.90° to 15.36° as shown in Fig. 1(a). This shifting could be attributed to the replacement of BDC ions from the interlayer region and coordinated to Zn(II) ions.[30] Generally speaking, the shifting of 2θ is linked to the change in lattice parameters, microstrain and crystal size.

The diffraction pattern of pure LDH exhibited characteristic peaks at 11.90°, 23.40°, 35.13°, 39.78°, 46.97°, 60.95°, and 62.90°, representing the (003), (006), (012), (015), (018), (110), and (113) crystal planes, respectively, which have been well indexed using a typical hexagonal MgAl-LDH (JCPDF 22-0452).[31] Characteristic diffraction peaks representing the LDH were evidently displayed in the XRD spectrum of MgAl-LDH/Zn-MOF. Diffraction peaks at 2θ = 6.59°, 9.81°, 15.36°, 26.59°, 35.78°, and 43.64° were observed for MgAl-LDH/Zn-MOF, which were assigned to (200) (220), (003), (006), (012), and (015) lattice planes. The presence of major diffraction peaks of Zn-MOF at 6.59° and 9.81° are assigned to the lattice planes of (200) and (220), respectively.[19,27] Interestingly, MgAl-LDH/Zn-MOF shows the shift in 2θ value to a higher angle, indicating the replacement of large BDC ions from the interlayer region.[29] The crystallite size of MgAl LDH and MgAl LDH/Zn-MOF nanocomposite was estimated as 15 nm and 38.46 nm, respectively, using Debye–Scherrer's eqn (4),[23] as follows.

$$D = k\,\lambda/\beta\cos\theta \quad (4)$$

where D is the crystallite size, k is Scherer's constant (0.98), λ is the wavelength (0.154 nm), β is the full width at half maximum (FWHM), and θ is the Bragg's angle. The d-line spacing was calculated using the following eqn (5).

$$d = n\lambda/2\sin\theta \quad (5)$$

where d is the line spacing, and n is the reflection order. The wavelength λ used in this calculation is 0.154 nm.

3.2. N_2 adsorption analysis at 77 K

The effect of the increased surface area on the characteristics of nanocomposites is an area of growing importance for understanding, developing, and improving materials for various applications, especially in adsorption.[32] The main objective of catalytic reactions is to increase the reaction rate while maintaining high product yield and selectivity.[33] This goal can be achieved by developing a composite that provides many active sites for adsorption processes.

The surface area and pore volume were examined using the multipoint Brunauer–Emmett–Teller (BET) method (Fig. 1(b)) to investigate the porosity of MgAl LDH/Zn-MOF. The average pore size for the nanocomposite was determined by the Dubinin–Astakhov (DA) plot, as shown in Fig. 1(b) (inset). The MgAl LDH/Zn-MOF composite was found to have a pore volume and an average pore radius of 0.045 $cm^3\ g^{-1}$ and 20.7 Å, respectively.

3.3. Morphology

The average grain size of the obtained MgAl LDH and MgAl LDH/Zn-MOF was determined using SEM, as shown in Fig. 1(c) and (d). The images reveal a flat, non-uniform, plate-like structure of MgAl LDH sheets lying in layers, with Zn-MOF particles organized as spherical aggregates and arranged on the MgAl LDH sheet, with an average grain size of 34.2 nm. The SEM image of Zn-MOF is given in Fig. S2c (ESI†). It is evident from the EDS study (Fig. 1(e)) that the MgAl-LDH/Zn-MOF structure contains significant amounts of Mg, Al, Zn, and O. However, a notable presence of carbon is attributed to the BDC anions.

3.4. FTIR spectral analysis

The FTIR spectra of the prepared samples, namely MgAl LDH and MgAl LDH/Zn-MOF, are presented in the ESI,† Fig. S1. The broad peak observed at 3459 cm^{-1} and 3520 cm^{-1} for MgAl LDH and MgAl LDH/Zn-MOF, respectively, corresponds to the stretching vibration of O–H due to the presence of water molecules. The sharp, weak peaks at 1559 cm^{-1} and 1572 cm^{-1} are attributed to O–H bending vibration and aromatic ring of BDC for MgAl LDH and MgAl LDH/Zn-MOF, respectively. The peaks 1050 cm^{-1}, 1097 cm^{-1}, and 1117 cm^{-1} presented the –C–OH, –C═O, and C–H groups of BDC. In addition, the vibrational peaks observed between 400 cm^{-1} to 800 cm^{-1} correspond to the stretching peaks of M–O–M and O–M–O vibrations, representing the Mg–O–Mg and Al–O–Al layers. The vibrational peak[34–36] observed near 400 cm^{-1} confirms the presence of zinc in MgAl LDH/Zn-MOF, as shown in ESI† (Fig. S1). The FTIR spectrum of Zn-MOF (Fig. S1, ESI†) confirms the synthesis of this material.

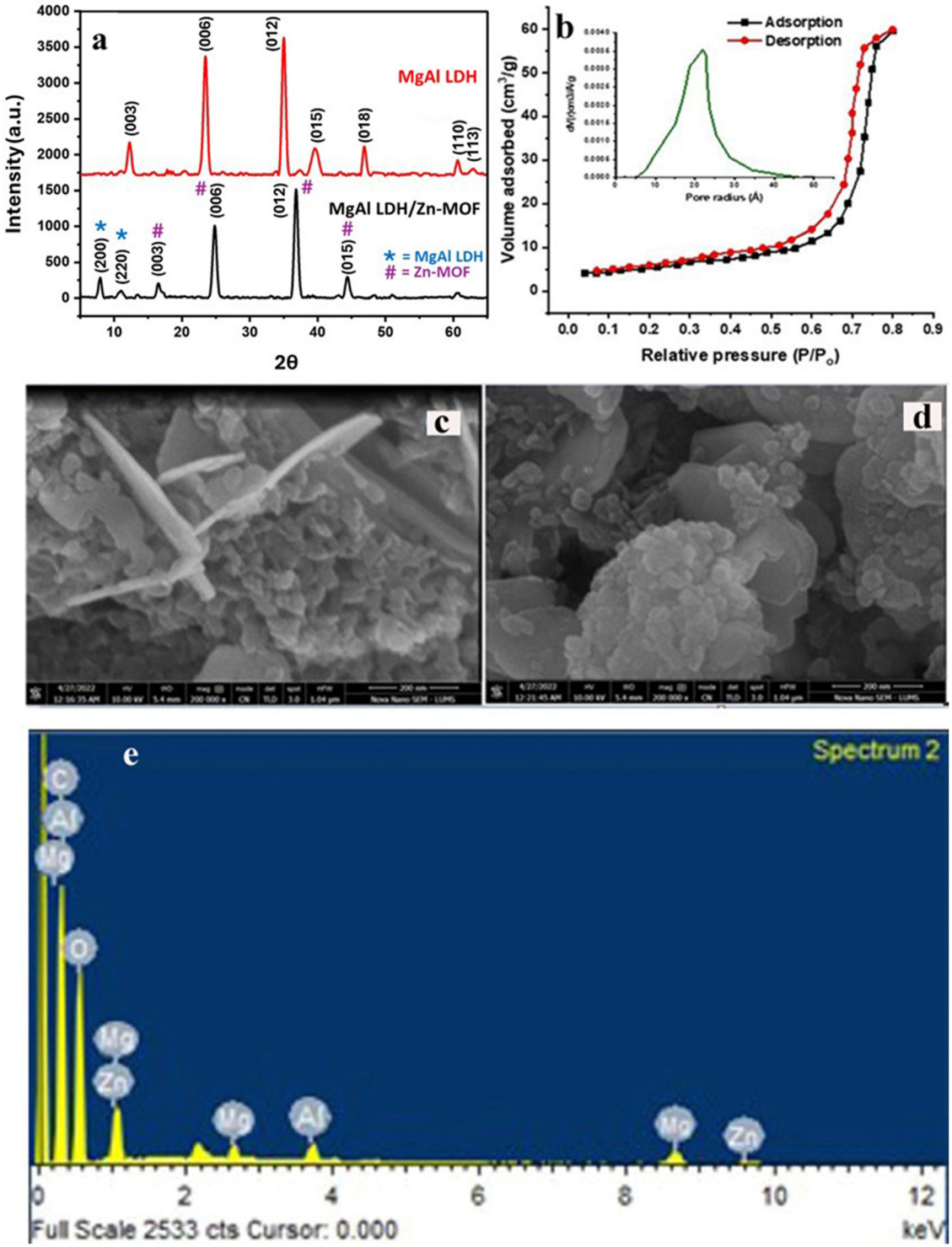

Fig. 1 (a) XRD diffractograms of the prepared MgAl LDH and MgAl LDH/Zn-MOF; (b) N_2 adsorption analysis at 77 K of MgAl LDH/Zn-MOF (pore size distribution in inset); (c)–(d) SEM images of MgAl LDH and MgAl LDH/Zn-MOF; (e) EDS spectrum of MgAl-LDH/Zn-MOF.

3.5. Optical properties of the resulting samples

3.5.1. UV-vis absorption analysis. The UV-vis spectra of MgAl LDH and MgAl LDH/Zn-MOF in the range of 200–500 nm are displayed in ESI† (Fig. S1b). The spectrum of MgAl LDH exhibits two distinct peaks at 230 nm and 259 nm, which correspond to the π to π* and n to π* transitions of the aromatic C═C and C═O bonds in the Zn-MOF. On the other hand, the electronic transitions of MgAl LDH/Zn-MOF are observed at higher wavelengths of 270 nm and 329 nm, which correspond to the π to π* and n to π* transitions of the BDC ligand. This red

shift in the electronic transitions can be attributed to the decreased π electron density of Zn metal. The weak absorbance observed in the UV spectra of MgAl LDH/Zn-MOF can be attributed to the irregular arrangement of BDC anions. Moreover, the weak transition of C=O observed in the spectrum of MgAl LDH/Zn-MOF indicates the intercalation of BDC anions into zinc metal.[30] The presence of a peak at ≈373 nm in the UV-vis spectrum (Fig. S2b, ESI†) of Zn-MOF confirms its synthesis.

3.5.2. UV-vis diffuse spectral analysis. When a semiconductor is exposed to a sufficient amount of energy, it undergoes electron transition, resulting in the generation of a photogenerated electron–hole pair. This pair exhibits strong reduction and oxidation activity, triggering the photocatalytic reaction.[37] Thus, the semiconductor's ability to absorb visible light plays a crucial role in its application in photocatalysis. In the case of MgAl LDH, its UV-vis diffuse reflectance spectroscopy demonstrates a broad peak at 400–600 nm, which indicates that the catalyst can effectively utilize visible light (Fig. 2(a)). Additionally, the coupling of MgAl LDH into Zn-MOF in the form of MgAl LDH/Zn-MOF (red shift) is believed to impact light absorption positively. For the preparation of a good photocatalyst, a reasonable band gap is a prerequisite, and the band gap value is one of the critical parameters of a semiconductor. Based on the Kubelka–Munk (eqn (6)) method.[38]

$$\propto h\nu = A(h\nu - E_g)^{n/2} \quad (6)$$

(where α represents the absorption coefficient, $h\nu$ is the photon energy, and E_g is the band gap energy). The energy band gap of the aforementioned samples is demonstrated in Fig. 2(b). The band gaps of 1.85 and 1.95 eV correspond to Zn-MOF and MgAl LDH, respectively. Consequently, visible light can activate both Zn-MOF and MgAl LDH to create photogenerated holes and electrons, which exhibit strong oxidation and reducibility, thereby promoting the photocatalytic reaction.[20,39] Upon coupling the Zn-MOF and MgAl LDH into MgAl LDH/Zn-MOF results in a significant decrease the band gap (1.47 eV) which is attributed to minimum interfacial resistance and maximum yield of H_2 production.

3.6. Zeta potential and point of zero charge (PZC)

The stability of MgAl LDH/Zn-MOF was evaluated by measuring its zeta potential, which is displayed in Fig. 2(c). The zeta potential measures the electrostatic repulsion between particles and is indicative of their tendency to aggregate and overall stability.[40] The average zeta potential of MgAl LDH was approximately 14.92 mV, while Zn-MOF had an average zeta potential of about −22.42 mV. On the other hand, the zeta potential of MgAl LDH/Zn-MOF was around 3.35 mV, which is intermediate between that of Zn-MOF and MgAl LDH. This phenomenon occurs due to the presence of opposite surface potentials between MgAl LDH and Zn-MOF, which strengthens the coupling force between them. Zn-MOF, being larger in size and having a negative surface zeta potential, indicating the formation of a new catalyst distinct from either MgAl LDH or Zn-MOF. This process enhances the proton absorption of MgAl LDH/Zn-MOF and promotes the efficiency of hydrogen evolution under visible light.

The pH point of zero charges (pHpzc) is a measurement that reveals the adsorption capacity of an adsorbent and the type of its surface-active center. Essentially, the pHpzc value of an adsorbent indicates the pH at which the adsorbent surface has no net charge.[41] When the number of positive and negative charges are equal, an adsorbent's surface reaches a zero point of charge (PZC), meaning it has no preference for attracting either positively or negatively charged substances. To determine the PZC, pH initial vs pH final plot is done and the point of intersection is identified, which is 7.1 in Fig. 2(d). This value is significant because it is the pH at which the adsorbent's surface carries no net charge, allowing it to adsorb/attract both positively and negatively charged substances equally.

3.7. Hydrogen evolution measurements

The present study compares the hydrogen evolution properties of two materials, namely magnesium–aluminum layered double hydroxide (MgAl LDH) and zinc-based metal–organic framework (Zn-MOF). The reaction occurs under visible light irradiation in a robust environment with a pH level of 10 (Fig. 3(a)–(f)). The photocatalytic hydrogen generation activity of both materials is low when used separately due to poor electron–hole pair separation and transfer efficiency under light. It has been discovered that when MgAl LDH and Zn-MOF are combined, they exhibit significantly better photocatalytic activity compared to when any of the materials is used alone. This suggests that there is a strong interaction between the two materials which leads to better hydrogen evolution. The yields for Zn-MOF and MgAl LDH are 85.07 mmol and 27.82 mmol, respectively. In contrast, the combined material MgAl LDH/Zn-MOF demonstrated hydrogen evolution activities that were 1.52 and 4.65 times higher than those of Zn-MOF and MgAl LDH alone, respectively. We have compared the effectiveness of MgAl LDH/Zn-MOF photocatalyst with various other MOF-based photocatalysts that have been previously reported in literature. The results of these comparisons are tabulated in ESI† (Table S1).

The superior photocatalytic activity of MgAl LDH/Zn-MOF can be attributed to the rapid separation and migration of charge carriers induced by visible light. This is facilitated by the strong interaction between the two materials. Additionally, the incorporation of MgAl LDH improves the light absorption of Zn-MOF, while the incorporation of Zn-MOF helps to prevent the agglomeration of MgAl LDH nanolayers, thus assisting in electron migration during photocatalytic water-splitting reactions. These findings demonstrate that the MgAl LDH/Zn-MOF composite has promising potential for use as a photocatalyst in various applications, including hydrogen production and environmental remediation.

The combination of MgAl LDH and Zn-MOF creates an S-scheme heterojunction which enhances the separation efficiency of electron–hole pairs in space. This leads to a higher efficiency in generating photocatalytic hydrogen compared to using the materials individually. The hydrogen evolution

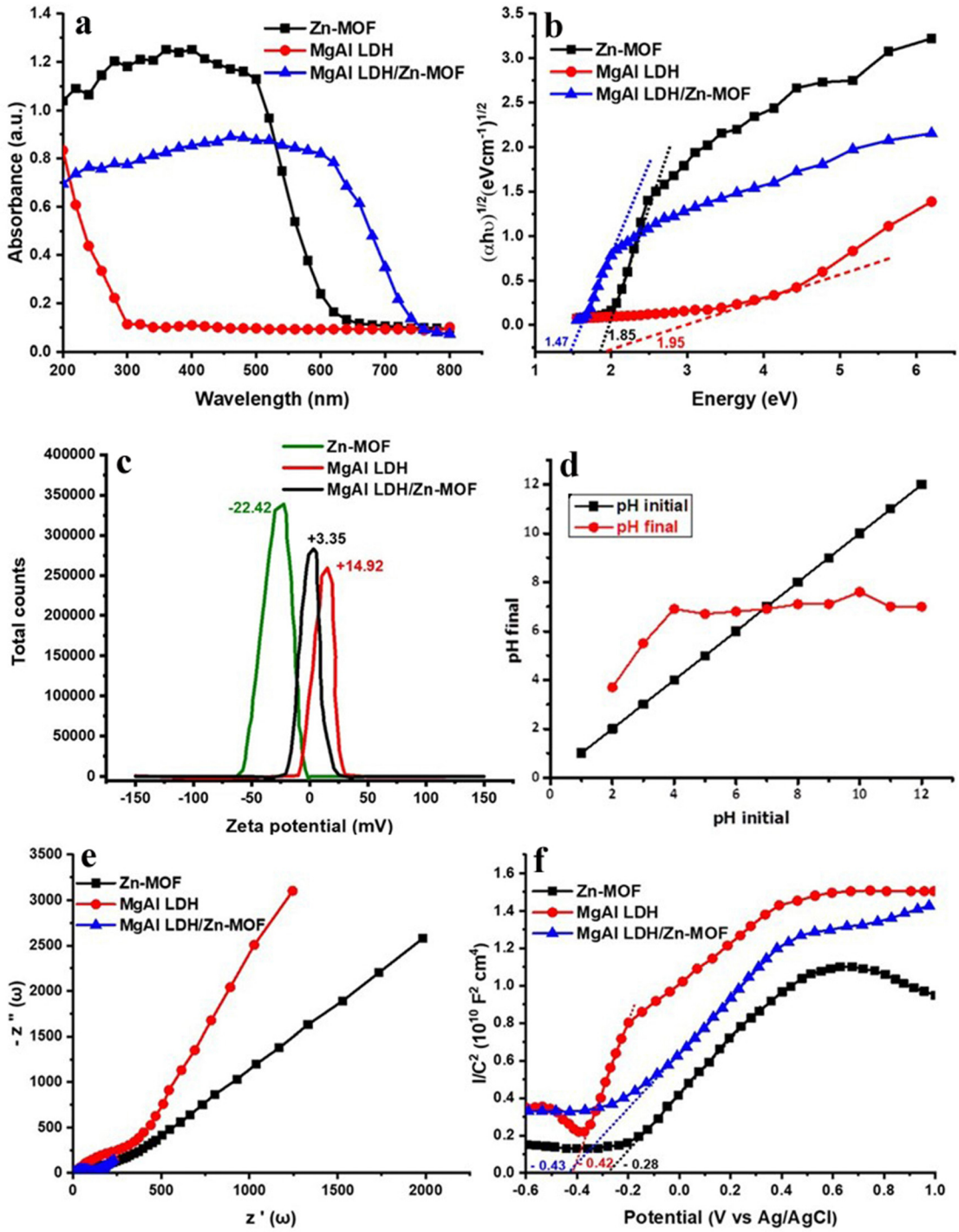

Fig. 2 (a) UV-vis DRS spectra, (b) band gap determination and (c) zeta potential of MgAl LDH, Zn-MOF and MgAl LDH/Zn-MOF. (d) Point of zero charge value of MgAl LDH/Zn (BDC) MOF; (e) EIS and (f) Mott–Schottky plots of Zn-MOF, MgAl LDH, and MgAl LDH/Zn-MOF.

mechanism section will provide detailed information on the specific migration process of light-excited electrons between MgAl LDH and Zn-MOF. To ensure the stability of MgAl LDH/Zn-MOF, EY was added in 5 mg increments in each cycle, to avoid any excessive shielding effects on the photocatalytic activity of hydrogen evolution (Fig. 3(c)). The experiment was conducted over five consecutive testing phases, where the photocatalyst was collected, washed, and dried after each cycle. The MgAl LDH/Zn-MOF demonstrated a consistent H_2 production rate of 112 mmol g^{-1} even after five cycles, proving its good reusability. The research findings suggest that the combination of MgAl LDH and Zn-MOF results in a highly stable photocatalyst that can efficiently generate hydrogen through long-term photocatalysis. The study highlights the significant role of

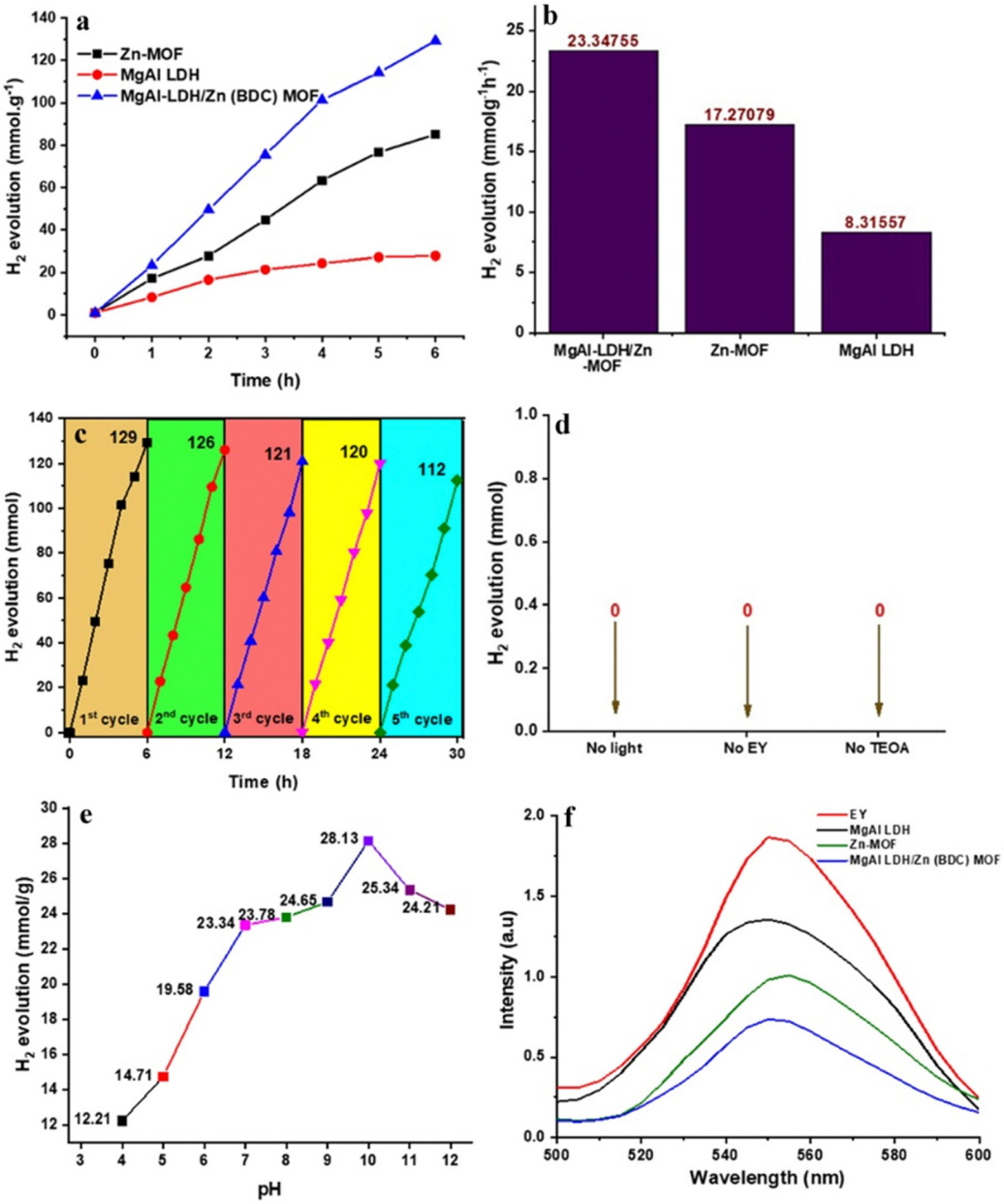

Fig. 3 (a) H_2 evolution activity of MgAl LDH, Zn-MOF, and MgAl LDH/Zn-MOF samples in mmol g^{-1}; (b) H_2 evolution in 1 h; (c) Stability testing of MgAl LDH/Zn-MOF; (d) hydrogen evolution of MgAl LDH/Zn-MOF in different reaction conditions; (e) H_2 evolution at different pH values; (f) steady-state fluorescence spectrum of EY, MgAl LDH, Zn-MOF, and MgAl LDH/Zn-MOF.

EY in the process of photocatalytic water-splitting to evolve hydrogen. Moreover, the hydrogen evolution activity of the catalyst was tested under different reaction conditions, which revealed its strong selectivity for hydrogen evolution systems. It was observed that the catalyst is unable to produce hydrogen in the absence of light, EY, or TEOA. These findings are illustrated in Fig. 3(d), which demonstrates the dependence of hydrogen evolution on the presence of light, EY, and TEOA. The pH of a solution affects hydrogen generation activity. To test this, 10% TEOA (sacrificial agent) was taken along with different acidity levels (using HCl/NaOH) in the solution. The results (Fig. 3(e)) show that the hydrogen production rate decreases in acidic solutions, and the best pH level for producing hydrogen is 10. If the pH level is too high, the hydrogen production rate also decreases due to defects in the photocatalyst surface. Additionally, when too many OH^- ions are present, they can react with photogenerated H^+ ions to produce water, slowing hydrogen production. The fluorescence spectra of three catalysts (MgAl LDH, Zn-MOF, and MgAl LDH/Zn-MOF) were examined to understand the separation and transfer of charge carriers in the MgAl LDH/Zn-MOF heterojunction catalyst (as shown in Fig. 3(f)). The fluorescence emission intensity of EY is an indicator of the recombination of electron–hole pairs. The results show that when the catalyst

samples are introduced, there is a decrease in fluorescence emission intensity, indicating a reduction in the recombination of electron–hole pairs. It appears that there is a strong interaction between EY and the catalyst, resulting in the reduction of fluorescence when EY was exposed to light. The addition of MgAl LDH/Zn-MOF heterojunction catalyst results in the lowest fluorescence emission intensity. This is a sign of successful design and construction of the S-scheme heterojunction, which facilitated charge migration and effectively prevented the recombination of electron–hole pairs. As a result, the hydrogen evolution activity is significantly enhanced. In order to evaluate the effectiveness of the synthesized photocatalysts, it is necessary to determine their catalytic efficiency. The turnover number (TON)[42] can be used as a metric for this purpose, and it can be calculated using eqn (7). The TON values of Zn-MOF, MgAl LDH, and MgAl LDH/Zn-MOF are 1.4, 4.3, and 6.5 respectively, while the rate of H_2 production is 8.32, 17.27, and 23.34 mmol g^{-1} h^{-1} respectively (Fig. 3(b)).

$$\mathrm{TON} = \frac{(\text{moles of } H_2 \text{ production})}{(\text{weight of used photocatalyst})} \quad (7)$$

3.7.1. Tracing the electron transfer process in S-scheme. Metallic materials can serve as a valuable means of detecting gains and losses in electron transfer due to their ability to provide a significant number of free electrons.[43] To assess the trend of interfacial charge transfer in the MgAl LDH/Zn-MOF photocarrier at the interface of as-fabricated Zn-MOF and MgAl LDH catalysts, a photoelectrochemical (PEC) study was conducted using EIS, as depicted in Fig. 3(e). The MgAl LDH/Zn-MOF composites have a semicircular diameter smaller than that of both MgAl LDH and Zn-MOF. Due to this, the MgAl LDH/Zn-MOF has the smallest radius, resulting in the least amount of interfacial resistance. This characteristic is beneficial for the transfer of interfacial charges.[44,45]

The results from zeta potential, fluorescence, and EIS studies support the superior hydrogen evolution performance of MgAl LDH/Zn-MOF catalysts. The Mott–Schottky curve indicates that Zn-MOF's flat band potential (E_{fb}) is approximately −0.28 V *versus* Ag/AgCl, while MgAl LDH's is −0.42 V (Fig. 3(f)). All MgAl LDH, Zn-MOF, and MgAl LDH/Zn-MOF samples all exhibit positive slopes, indicating that they have n-type semiconductor characteristics.[46,47] In addition, for n-type semiconductors, the conduction band potential (E_{CB}) is typically negative[48–50] by about 0.2 V, compared to the E_{fb}. Therefore, it can be confirmed that the E_{CB} of Zn-MOF and MgAl LDH are −0.48 V and −0.62 V, respectively. Valence band positions (E_{VB}) were determined (eqn (8)) using UV-VIS/DRS (Fig. 3(b)) and M–S techniques (Fig. 3(f)), as mentioned in the literature.[49,51] Notably, the M–S findings provided substantial evidence to clarify the electron transfer mechanism discussed in this study.[51]

$$E_{VB} = E_{CB} + E_g \quad (8)$$

The terms E_{CB} and E_{VB} refer to the potential of the conduction and valence bands, respectively. The E_{VB} values of Zn-MOF and MgAl LDH were calculated as 1.37 and 1.33 eV, respectively. To confirm the absolute position of E_{VB} for Zn-MOF and MgAl LDH, UPS spectra (Fig. 5(a)) were obtained. The low binding energy area (valence band region near the Fermi level) was observed to calculate the valence band position.[52–54] The measured E_{VB} values are 1.325 eV for Zn-MOF and 1.366 eV for MgAl LDH. These results agree with the above calculated E_{VB} values.

It has been verified through charge analysis of the band that the formation of an intrinsic electric field (IEF) was facilitated at the interface by electron transfer of 0.04 eV from MgAl LDH to Zn-MOF, which resulted in the participation of photogenerated electrons in the hydrogen production process. The Zn-MOF/MgAl LDH heterojunction allows for the movement of electrons from VB to CB because both materials are UV-vis-responsive semiconductors.[55] The irradiation facilitates this process (Fig. 4). Afterward, the excited electrons on the weakly reducing Zn-MOF combine with the excited holes on the weakly oxidizing MgAl LDH. The retention of photoexcited solid electrons and holes in the composite of MgAl LDH/Zn-MOF allows the creation of an S-scheme heterojunction.[56] Through experimental results, the generation of IEF is demonstrated while also confirming the charge separation path of the S-scheme heterojunction.[55]

The transfer of charge in a heterojunction of S-scheme can be described in the following way.[57,58]

(1) Fig. 4 indicates that MgAl LDH has a higher CB and VB position and a more minor work function than Zn-MOF. When these two semiconductors are nearby, electrons in MgAl LDH diffuse spontaneously to Zn-MOF, creating an electron depletion layer and an electron accumulation layer near the interface of MgAl LDH and Zn-MOF, respectively. Electrons are transferred to Zn-MOF, causing it to be negatively charged, while MgAl LDH becomes positively charged. This generates an electric field from MgAl LDH to Zn-MOF, which facilitates the movement of photogenerated electrons from Zn-MOF to MgAl LDH.

(2) The alignment of Fermi energy is necessary when Zn-MOF and MgAl LDH come into contact. This alignment causes the Fermi levels of Zn-MOF to shift upwards and those of MgAl LDH to shift downward. As a result of the band-bending effect, the photogenerated electrons in the CB of Zn-MOF and holes in the VB of MgAl LDH tend to recombine at the interface region. This phenomenon can be easily understood by the analogy of water flowing downhill.

(3) The interface between the CB of Zn-MOF and the VB of MgAl LDH causes photogenerated electrons and holes to recombine due to Coulombic attraction. The internal electric field, band bending, and Coulombic attraction drive the recombination. During this process, unnecessary electrons and holes are removed. However, the potent photogenerated electrons in the CB of MgAl LDH and the holes in the VB of Zn-MOF are preserved for the purpose of photocatalytic reactions.[59–61]

3.7.2. Mechanism analysis of hydrogen evolution reaction. Fig. 4 shows a simplified explanation of the internal migration mechanism of the MgAl LDH/Zn-MOF S-scheme heterojunction for hydrogen production activity. The MgAl LDH has a higher

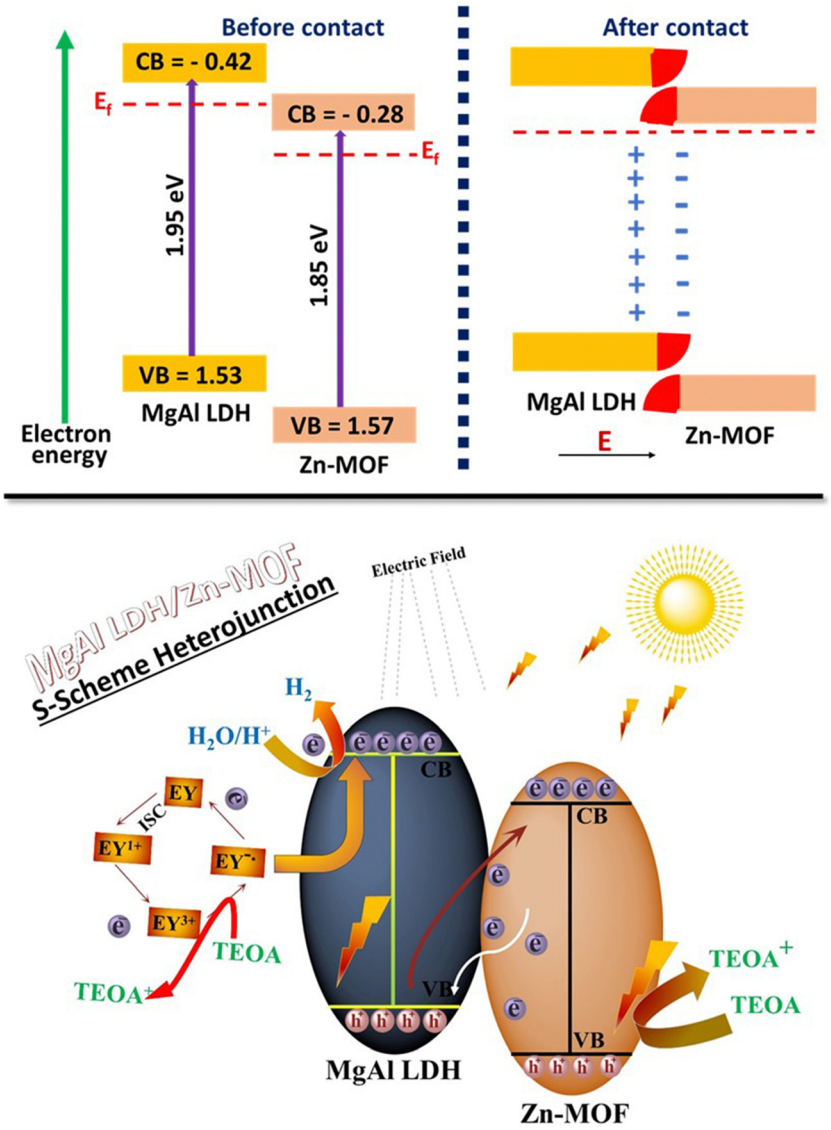

Fig. 4 The internal mechanism of migration of electrons within the MgAl LDH/Zn-MOF heterojunction in the S-scheme.

conduction band (CB) and valence band (VB) position, as well as a smaller work function in comparison to the Zn-MOF. When the two materials come in contact, the electrons in MgAl LDH will spontaneously diffuse to the Zn-MOF, creating electron depletion and accumulation layers near their interface. This results in the formation of an internal electric field that will direct the transfer of photogenerated electrons from the Zn-MOF to MgAl LDH. The Fermi energy levels of Zn-MOF and MgAl LDH align to the same level when they come into contact. Consequently, this leads to upward and downward shifts in the Fermi levels of Zn-MOF and MgAl LDH, respectively. Band bending facilitates the recombination of photogenerated electrons in the conduction band of Zn-MOF and holes in the valence band of MgAl LDH at the interface region due to the Coulombic attraction between the holes and electrons. The internal electric field, band bending, and Coulombic attraction act as driving forces for the recombination of electrons in the CB of Zn-MOF and holes in the VB of MgAl LDH. This eliminates the useless electrons and holes *via* recombination, while preserving the powerful photogenerated electrons in the CB of MgAl LDH and the holes in the VB of Zn-MOF for photocatalytic reactions. The aggregated holes on the VB of Zn-MOF are immediately consumed by the sacrificial reagent TEOA. Simultaneously, the ground-state EY molecule is excited, forming the excited-state EY (EY^{-}). The charges from EY^{-} mainly transfer to the CB of MgAl LDH due to the strong competition between the energy levels of MgAl LDH and Mg-MOF. The reduction potential of the CB of MgAl LDH is stronger than that of Zn-MOF. Finally, the electrons on the CB of MgAl LDH combine with H^+ to produce H_2.

3.8. Dye removal experiments

The present study displays the UV-visible spectra of a freshly prepared aqueous solution of MR. It is characterized by a

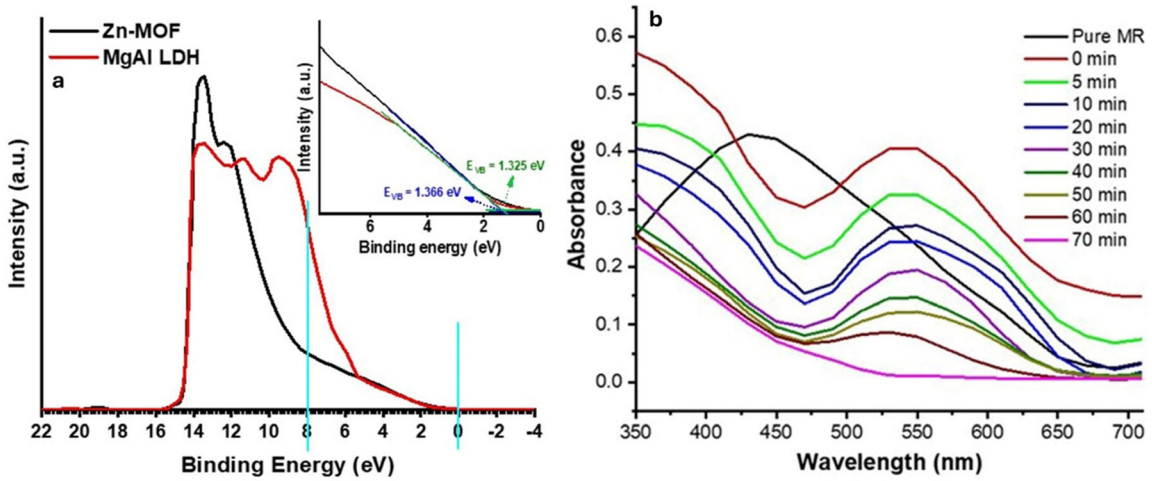

Fig. 5 (a) He I UP spectra of Zn-MOF (black) and MgAl LDH (red). Inset – zoom on the low BE area (valence band region near the Fermi level) for estimation of EVB, (b) UV-vis spectra of MR degradation in this presence of MgAl LDH/Zn-MOF nanocomposite.

dominant absorption band at 431 nm, as demonstrated in Fig. 5(b). When MgAl LDH/Zn-MOF is added to the solution, the peak shifts from 431 nm to 538 nm, resulting in a redshift of approximately 107 nm. Interestingly, the addition of MgAl LDH/Zn-MOF also changes the color of the solution from yellow to red and the pH from 6.7 to 5.0 (Fig. 6(a)). The decrease in intensity over time is due to the adsorption of MR with MgAl LDH/Zn-MOF. The absorption peak in the visible region is caused by the chromophore, which includes the azo linkage (–N═N–). This is due to the n → π* transition that occurs because of the –N═N– group. At least three adsorption experiments were conducted to ensure data accuracy and reproducibility. Blank experiments were also conducted in parallel and corrected as needed.[56]

3.9. Factors affecting the adsorption process

3.9.1. Effect of pH on the adsorption capacity. In order to investigate the adsorption capacity of the prepared adsorbent for MR dye, experiments were conducted at various pH values ranging from 2 to 12. An adsorbent dose of 25 mg was used with a dye solution concentration of 25 ml. The pH of the solution was adjusted by adding either HCl or NaOH solution. The maximum adsorption capacity of the MgAl LDH/Zn-MOF composite was observed at pH 8 (Fig. S3a, ESI†), which can be attributed to the interaction between the negatively charged MR dye and the positively charged surface of the MgAl LDH/Zn-MOF. At higher pH values, an increase in the concentration of OH^- ions on the adsorbent's surface led to repulsion between the adsorbent and the methyl red dye, decreasing the adsorption capacity.[62] On the other hand, adsorption capacity decreased at acidic pH due to the dissolution of the adsorbent at lower pH values.

3.9.2. Effect of adsorption dose. In order to determine the effect of adsorbent amount on the adsorption capacity, various amounts of MgAl LDH/Zn-MOF adsorbent (50 mg, 75 mg, 100 mg, 125 mg, 150 mg and 175 mg) were tested with a 5×10^{-5} M aqueous dye solution. Results showed that the adsorption capacity of the adsorbent increased with the amount of adsorbent used (Fig. S3b, ESI†). This can be attributed to the increase in available adsorption sites, providing more opportunities for the dye molecules to adsorb onto the surface of the adsorbent. However, a point of adsorption saturation was reached, as no further increase in adsorption capacity was observed with increasing adsorbent amount. This is likely due to the complete adsorption of MR onto the surface of the adsorbent.[63]

3.9.3. Effect of concentration of dye on adsorption capacity of adsorbent. The percentage removal of the synthesized MgAl LDH/Zn-MOF composite at varying concentrations of MR dye is given in Fig. S3c (ESI†). The experiment used 25 mg of the composite in MR dye solutions of different concentrations ranging from 5 to 50 mg while keeping other reaction conditions constant. The maximum adsorption capacity was achieved by increasing the amount of MR dye up to 30 mg. However, the adsorption capacity of the adsorbent decreased as the amount of MR dye further increased. This decrease in adsorption capacity was due to the lack of further interaction between dye molecules and active sites on the adsorbent. As the MR dye concentration increases, the active sites of the adsorbent are not enough to accommodate all the dye particles. So, adsorption capacity and percentage removal decrease with increased MR concentration.

3.9.4. Effect of time. A comparison of the adsorption performance of the prepared adsorbents was carried out over varying time intervals. As shown in Fig. S3d (ESI†), the adsorbents' removal efficiency increased with the experiment's duration, with a maximum removal percentage of 79% observed after 3 h of reaction time for MgAl LDH/Zn-MOF. The adsorption rate of MR dye on the surface of the adsorbent was fast, leading to an increased removal rate. However, after a certain point, the process became slower due to the establishment of equilibrium and a decrease in available adsorption sites. Therefore, the removal efficiency of MR dye gradually decreased after 3 h of reaction time.

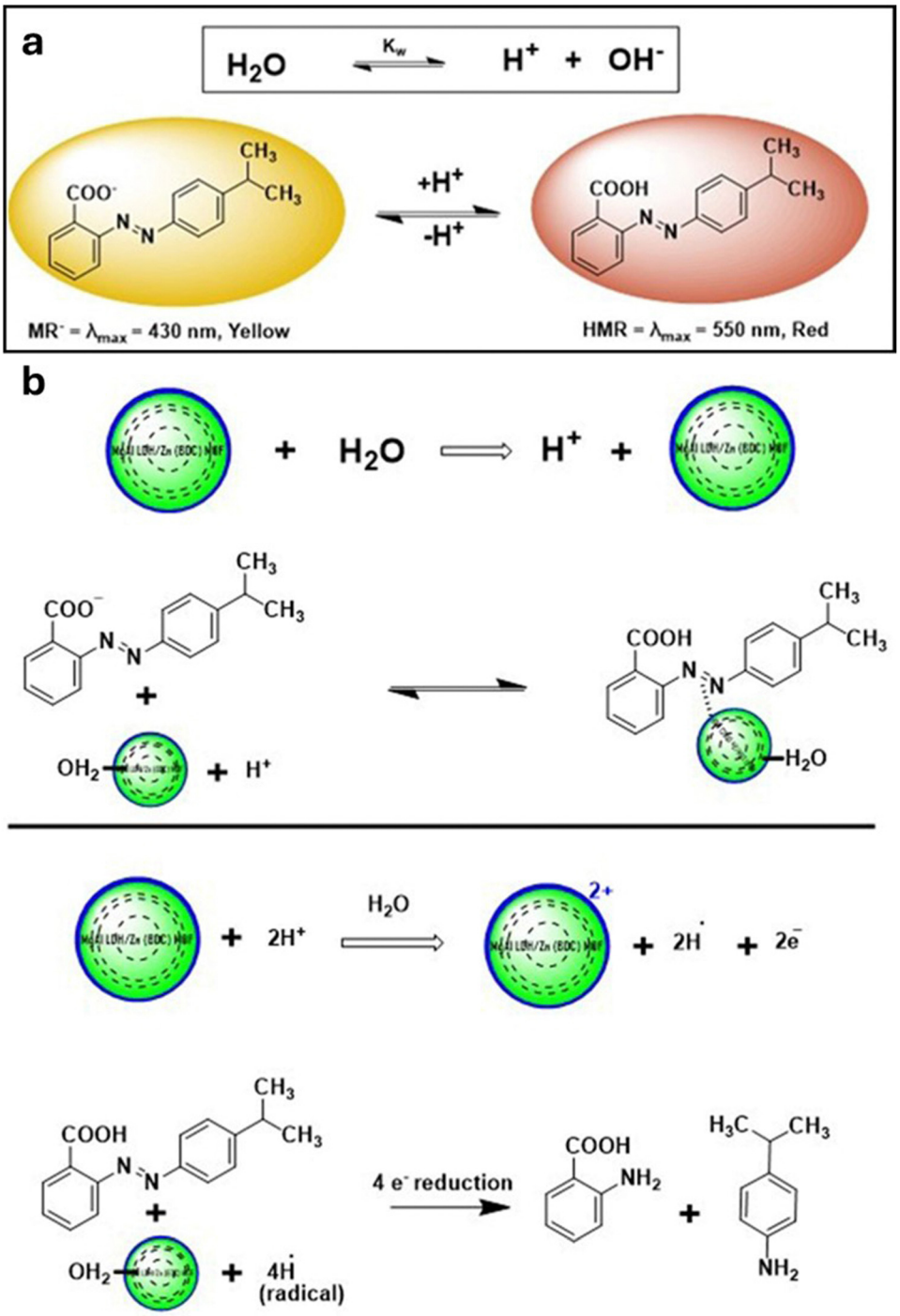

Fig. 6 (a) At 25 °C, the presence of HMR and MR^- species in water. (b) Degradation mechanism of MR by MgAl LDH/Zn-MOF.

3.9.5. Effect of co-existing ions. Dye-contaminated wastewater often contains a substantial amount of salt, which makes it more likely to compete with other anions for adsorption sites. As shown in Fig. S4 (ESI†), the presence of carbonate and sulphate noticeably affects the removal process, whereas chloride presence in water does not impact the adsorption process substantially. The lowest dye removal efficiency is found in the case of CO_3^{2-} ions which infers that CO_3^{2-} is more competitive compared to other anions. The reason behind this phenomenon can be explained by the alteration in the pH level of the solution and the tendency of the co-ion to bind with the active site of the adsorbent material.[64,65]

3.10. Comparison with other studies

In ESI,† Table S2 shows a compilation of literature results regarding the adsorption of MR using different adsorbents. While many studies focus on the degradation of MR, it is noteworthy that our investigation revealed a maximum degradation

efficiency of 98% using nanocomposites synthesized by the calcination method, which is associated with the significant drawback of lower yields. Considering the limitations of synthetic catalyst methods, degradation time, and degradation efficiency, MgAl LDH/Zn-MOF nanocomposites synthesis is a highly productive and demanding approach.

3.11. Mechanism of MR removal

There are two possible mechanisms for removing MR, and we will discuss each of them below.

(1) Adsorption is a process that involves the transfer of electrons between the adsorbent surface and the substance being adsorbed, resulting in the formation of a bond between the two.[66] The strength of this bond between the adsorbent and the adsorbate can significantly impact the chemisorption energy required for the process. The adsorption process is inherently slow and requires equilibrium to be reached, typically resulting in a single layer of adsorbate on the surface of the adsorbent. An efficient adsorbent must exhibit high adsorption kinetics, resilience to various conditions such as high pressure and temperature and require minimal maintenance.[67] Regarding MR dye, the molecules are adsorbed on the surface of the adsorbent and diffuse to the inner portion. The adsorption process depends on various factors, such as bonding type, surface interactions, and adsorbent nature. A variety of kinetic models, including pseudo-first-order kinetics, pseudo-second-order kinetics, liquid-film diffusion model, and intra-particle diffusion model, have been used to evaluate the mechanistic studies of the adsorption of MR dye on the surface of the hybrid composite that has been fabricated. Table S3 (ESI†) presents the values obtained from these kinetic models, which confirm that the current adsorption mechanism is chemisorption.[68,69]

(2) MR is used as a pH indicator, and it is crucial to thoroughly examine their reactive and predominant species. In aqueous solutions, the presence of –COOH and –N=N– groups leads to a balance between HMR and MR^- species. Fig. 6(b) shows the Fenton-like reaction of MgAl LDH/Zn-MOF in an aqueous solution, which generates hydrogen ions. The adsorption of MR onto the surface of MgAl LDH/Zn-MOF was observed to cause a remarkable shift of λ_{max} from 431 nm to 538 nm, which can be attributed to the protonation of the dye. This finding stands as the most significant outcome of the study, as depicted in Fig. 5(b). The reaction of MgAl LDH/Zn-MOF with H_2O and/or H^+ generates hydrogen radicals as shown in Fig. 6. According to Florence, the reduction of aromatic azo compounds is a four-electron process that results in the formation of corresponding aromatic amines *via* an unstable intermediate, hydrazobenzene (–NH–NH–), which is more labile than the parent –N=N– compound.[70] The multi-electron transfer oxidation–reduction mechanism (Fig. 6(b)) observed in the MgAl LDH/Zn-MOF complex is in complete agreement with the previous findings.[71] The azo double bond (–N=N–) was successfully transformed into $–NH_2$, resulting in a gradual decrease in the visible absorption peak of MR at 538 nm over time. Throughout the process, it is worth noting that MgAl LDH/Zn-MOF played a crucial dual role. Specifically, it was able to generate hydrogen radicals while simultaneously transferring these radicals to the MR *via* the electron relay effect. Fig. 6(b) mechanism strongly supports the proposals of Miller *et al.* regarding the catalytic reduction of water on the surface of a colloidal metal.[72] Unfortunately, we did not find any degraded product on the surface of MgAl LDH/Zn-MOF.

3.12. Results for kinetics and adsorption studies

Various models, including pseudo-first-order kinetics, pseudo-second-order kinetics, liquid-film diffusion model, and intra-particle diffusion model, were used to study the adsorption kinetics and isotherms of MR dye on MgAl LDH/Zn-MOF. The experimental data were best fitted by the intra-particle diffusion model, which yielded an impressive R^2 value of 0.996. Therefore, it can be confidently concluded that the intra-particle diffusion model is the most suitable to explain the adsorption behavior of MR dye on MgAl LDH/Zn-MOF (Table S3, ESI†). This suggests that the adsorption of MR dye molecules on the surface of the adsorbent and their diffusion into the inner pores are facilitated by electron transfer and the creation of bonding between them.

The fitting of various kinetic models to the adsorption data is given in Fig. S5 (ESI†). In addition, different adsorption isotherms (Fig. S6, ESI†), including Langmuir, Freundlich, and Temkin, were evaluated to describe the adsorption behavior of MR dye on the prepared adsorbent. The Freundlich isotherm model best fits the experimental data, with an R^2 value of 0.957 (Table S4, ESI†) and a higher adsorption capacity of 254.8 mg g^{-1} of MR dye on MgAl LDH/Zn-MOF. The straight line obtained for the isotherm models indicates that the adsorption behavior is consistent with monolayer adsorption.

3.13. Thermodynamic study of MR dye adsorption

The adsorption process is known to be dependent on temperature. In this study, the thermodynamic behavior of the adsorption of MR dye on MgAl LDH/Zn-MOF was also examined. The adsorption increased with increasing temperature from 303 K to 343 K, which was attributed to the increase in the value of K_L. Table S5 (ESI†) presents the values of different thermodynamic parameters obtained from the study. A straight line was obtained by plotting the graph between $\ln K_L$ and $1/T$, (Fig. S7a, ESI†). The values of ΔH° and ΔS° were deduced from the slope and intercept of the graph, respectively. It was concluded that the adsorption of MR dye was an endothermic, spontaneous process with enhanced randomness. The negative value of ΔG° indicated the thermal stability of the adsorption process. These results demonstrated that temperature played an essential role in the adsorption process and could be used to optimize the adsorption efficiency of MgAl LDH/Zn-MOF to remove MR dye.

3.14. Regeneration performance and magnetic properties of MgAl LDH/Zn-MOF

In experimental applications, one of the most critical elements is the adsorbent capacity for reuse. Adsorption–desorption

experiments were conducted to assess the reusability of MgAl-LDH/Zn MOF for MR dye removal. It is observed that the adsorption capacity of MR dye decreased slightly from 95.43% to 81.75% after five adsorption–desorption cycles (Fig. S7b, ESI†), indicating the adsorbent's reusability. However, the lower reduction rate after different cycles was due to incomplete desorption of MR dye from the adsorbent surface. Overall, the MgAl-LDH/Zn MOF exhibited a strong capacity for restoration and can be effectively used again to remove MR dye from contaminated water.

The observed hysteresis loop characteristics (Fig. S7c, ESI†) demonstrate that the MgAl LDH/Zn-MOF exhibits exceptional magnetic properties and superior recyclability. Notably, the saturation magnetization rate of the catalyst is approximately 54.26 emu g^{-1}, which represents a marked improvement over conventional heterogeneous catalysts that are difficult to recycle. The findings of this study suggest that the MgAl LDH/Zn-MOF is a promising catalyst with significant potential for industrial applications.

3.15. CO_2 adsorption capacity of MgAl LDH/Zn-MOF

In ESI† (Fig. S8), a cyclic process of CO_2 uptake and regeneration of the MgAl LDH/Zn-MOF is illustrated. The experiment was conducted at 298 K for 1 bar and 40 bar, for four cycles. The results indicate that the MgAl LDH/Zn-MOF composite exhibits excellent cyclic stability for CO_2 separation. It has fast adsorption and desorption kinetics, making it a promising candidate for removing CO_2 from gas streams. The CO_2 uptake of MgAl LDH/Zn-MOF was 5.89 cm^3 g^{-1} and 129.7 mg g^{-1}, respectively, at 1 bar and 40 bars. These findings suggest that this composite can effectively remove CO_2 from gas streams due to its reasonably high CO_2 uptake. Table S6 (ESI†) summarizes the CO_2 uptakes of both the adsorbents used in our study and those found in the literature. Our adsorbent (MgAl LDH/Zn-MOF) has shown exceptional performance in CO_2 adsorption, which is a significant achievement in this field. This development will pave the way for even more promising research and advancements in this area.

4. Conclusions

A new photocatalyst has been developed by combining two materials, Zn-MOF, and MgAl LDH, to form a special structure called MgAl LDH/Zn-MOF. This new structure effectively enhances electron and hole separation and promotes hydrogen evolution reaction under visible light. The light absorption performance of the Zn-MOF has been significantly enhanced by the addition of MgAl LDH. This photocatalyst is designed with a low steady-state fluorescence emission intensity and a high light-driven photocurrent response, which makes it highly effective in inhibiting the recombination of electron–hole pairs and significantly enhancing the photocatalytic hydrogen evolution reaction. To understand the exact mechanism of dye removal, various kinetic models and adsorption isotherms were studied. The results indicated that the intra-particle diffusion model and Freundlich isotherm model provided the most accurate fits to the experimental data, with maximum R^2 values of 0.996 and 0.957, respectively. These findings demonstrate that the MgAl LDH/Zn-MOF composite is a promising adsorbent for the removal of MR dye from contaminated water. Additionally, the study evaluated the adsorbent's capacity for reuse and showed that it can be employed multiple times with only a slight reduction in MR dye removal efficiency. The affinity between MgAl LDH and Zn-MOF shows a considerable adsorption capacity for carbon dioxide (CO_2). This strategic fusion of MOF architectures within LDH matrices presents a promising avenue for producing catalytic materials for an array of applications, such as air or liquid filtration, or medical applications.

Data availability statement

All data are present within the manuscript.

Author contributions

Ihsan Maseeh: writing – original draft, investigation; Farheen Anwar: writing – original draft, methodology, Sadia Aroob: writing – original draft; Tariq Javed: formal analysis; Ismat Bibi: formal analysis; Afaf Almasoudi: data curation; formal analysis; Ahmad Raheel: formal analysis. resources, investigation; Muhammad Arshad Javid: formal analysis; Sónia A. C. Carabineiro: visualization; writing – review & editing; Muhammad Babar Taj: writing – review & editing, project administration, supervision.

Conflicts of interest

Authors declare no conflicts of interest.

Acknowledgements

M. B. T. acknowledges support from HEC (Higher Education Commission) of Pakistan and thanks Dr Muhammad Imran (QAU) for help in the H_2 evolution activity. A. A. acknowledges support from King Abdulaziz University, P. O. Box 42734, Jeddah, Saudi Arabia. S. A. C. C. acknowledges support from FCT/MCTES, Fundação para a Ciência e Tecnologia and Ministério da Ciência, Tecnologia e Ensino Superior, DOIs: 10.54499/LA/P/0008/2020, 10.54499/UIDP/50006/2020, 10.54499/UIDB/50006/2020 and the Scientific Employment Stimulus – Institutional Call (DOI: 10.54499/CEECINST/00102/2018/CP1567/CT0026).

References

1 I. Jonek-Kowalska and R. Wolniak, *Smart Cities in Poland: Towards sustainability and a better quality of life?*, Taylor & Francis, 2023.

2 V. B. Singh, S. Madhav, N. C. Pant and R. Shekhar, *Weathering and Erosion Processes in the Natural Environment*, John Wiley & Sons, 2024.
3 A. Kozhukhova, S. du Preez and D. Bessarabov, *Int. J. Hydrogen Energy*, 2024, **51**, 1079–1096.
4 P. Hao, Z. Chen, Y. Yan, W. Shi and F. Guo, *Sep. Purif. Technol.*, 2024, **330**, 125302.
5 E. Fernandes, J. Gomes and R. C. Martins, *Catalysts*, 2022, **12**, 1218.
6 G. Manasa and C. S. Rout, *Mater. Adv.*, 2024, DOI: **10.1039/D3MA00362K**.
7 E. M. Abd El-Monaem, H. M. Elshishini, S. S. Bakr, H. G. El-Aqapa, M. Hosny, G. Andaluri, G. M. El-Subruiti, A. M. Omer and A. S. Eltaweil, *npj Clean Water*, 2023, **6**, 34.
8 M. E. Mahmoud, R. M. El-Sharkawy, E. A. Allam, G. M. Nabil, F. R. Louka, M. A. Salam and S. M. Elsayed, *J. Water Proc. Engineering*, 2024, **57**, 104625.
9 M. P. Jerome, F. A. Alahmad, M. T. Salem and M. Tahir, *J. Environ. Chem. Eng.*, 2022, **10**, 108151.
10 C. Li, J. Wang, L. Tong, Y. Wang, P. Zhang, M. Zhu and H. Dong, *Coord. Chem. Rev.*, 2024, **502**, 215623.
11 H. Lee, D. A. Reddy, Y. Kim, S. Y. Chun, R. Ma, D. P. Kumar, J. K. Song and T. K. Kim, *ACS Sustainable Chem. Eng.*, 2018, **6**, 16734–16743.
12 S. Das, S. Patnaik and K. Parida, *Inorg. Chem. Front.*, 2019, **6**, 94–109.
13 A. Sherryna and M. Tahir, *Int. J. Energy Res.*, 2022, **46**, 2093–2140.
14 A. Felix Sahayaraj, H. Joy Prabu, J. Maniraj, M. Kannan, M. Bharathi, P. Diwahar and J. Salamon, *J. Inorg. Organomet. Polym. Mater.*, 2023, 1–25.
15 G. A. Udourioh, M. Solomon, C. O. Matthews-Amune, E. Epelle, J. Okolie, V. E. Agbazue and U. Onyenze, *React. Chem. Eng.*, 2023, 278–310.
16 N. Yoshinari and T. Konno, *Coord. Chem. Rev.*, 2023, **474**, 214850.
17 A. I. Inamdar, S. Kamal, M. Usman, M.-H. Chiang and K.-L. Lu, *Coord. Chem. Rev.*, 2024, **502**, 215596.
18 W. Wang, M. Lin, W. Wang, Z. Shen and Z.-S. Wu, *Bioact. Mater.*, 2024, **33**, 279–310.
19 A. S. Elsherbiny, A. Rady, R. M. Abdelhameed and A. H. Gemeay, *Environ. Sci. Pollut. Res.*, 2023, **30**, 106860.
20 R. R. Ikreedeegh, S. Tasleem and M. A. Hossen, *Fuel*, 2024, **360**, 130561.
21 Z. Jin, Y. Li and Q. Ma, *Trans. Tianjin Univ.*, 2021, **27**, 127–138.
22 V. Şimşek, R. Z. Yarbay, V. Marttin and Ü. D. Gül, *J. Cleaner Prod.*, 2023, **421**, 138448.
23 S. Aroob, M. B. Taj, S. Shabbir, M. Imran, R. H. Ahmad, S. Habib, A. Raheel, M. N. Akhtar, M. Ashfaq and M. Sillanpää, *J. Environ. Chem. Eng.*, 2021, **9**, 105590.
24 S. Aroob, S. A. Carabineiro, M. B. Taj, I. Bibi, A. Raheel, T. Javed, R. Yahya, W. Alelwani, F. Verpoort and K. Kamwilaisak, *Catalysts*, 2023, **13**, 502.
25 L. Lu, J. Li, D. H. Ng, P. Yang, P. Song and M. Zuo, *J. Ind. Eng. Chem.*, 2017, **46**, 315–323.
26 S. G. Mtavangu, R. L. Machunda, B. van der Bruggen and K. N. J. S. R. Njau, *Sci. Rep.*, 2022, **12**, 15359.
27 Y. T. Dang, M.-H. D. Dang, N. X. D. Mai, L. H. T. Nguyen, T. B. Phan, H. V. Le and T. L. H. Doan, *J. Sci.: Adv. Mater. Devices*, 2020, **5**, 560–565.
28 A. S. Elsherbiny, A. Rady, R. M. Abdelhameed, A. H. J. E. S. Gemeay and P. Research, *Environ. Sci. Pollut. Res.*, 2023, **30**, 106860.
29 Z. Nazari, M. A. Taher and H. Fazelirad, *RSC Adv.*, 2017, **7**, 44890–44895.
30 A. Chakraborty and H. Acharya, *Colloid Interface Sci. Commun.*, 2018, **24**, 35–39.
31 H. Sun and S.-J. Park, *J. Ind. Eng. Chem.*, 2022, **111**, 183–191.
32 C. I. Idumah and C. M. Obele, *Surf. Interfaces*, 2021, **22**, 100879.
33 J. J. Villora-Picó, J. González-Arias, L. Pastor-Pérez, J. Odriozola and T. Reina, *Environ. Res.*, 2024, **240**, 117520.
34 N. Iyi, Y. Ebina and T. Sasaki, *J. Mater. Chem.*, 2011, **21**, 8085–8095.
35 F. Zhao, L. Fan, K. Xu, D. Hua, G. Zhan and S.-F. Zhou, *J. CO2 Util.*, 2019, **33**, 222–232.
36 B. S. Yadav and S. Dasgupta, *Inorg. Chem. Commun.*, 2022, **137**, 109203.
37 D. Umaru, H. Y. Hafeez, J. Mohammed, A. B. Suleiman, C. E. Ndikilar and Y. Zakariyya, *Appl. Surf. Sci.*, 2023, **18**, 100520.
38 J. Lee, W. K. Chong, S. H. W. Kok, B. J. Ng, X. Y. Kong, S. P. Chai and L. L. Tan, *Adv. Funct. Mater.*, 2023, **33**, 2303430.
39 S. Dharani, S. Vadivel, L. Gnanasekaran and S. Rajendran, *Fuel*, 2023, **349**, 128688.
40 R. Yan, S. Lin, W. Jiang, X. Yu, L. Zhang, W. Zhao and Q. Sui, *Sci. Total Environ.*, 2023, **898**, 165431.
41 E. Mosaffa, A. Banerjee and H. Ghafuri, *Environ. Sci.: Water Res. Technol.*, 2023, **9**, 2643–2663.
42 W. Raza, K. Ahmad and H. J. N. Kim, *Nanotechnology*, 2021, **32**, 495404.
43 F. Li, X. Yue, Y. Liao, L. Qiao, K. Lv and Q. J. N. C. Xiang, *Nat. Commun.*, 2023, **14**, 3901.
44 N. Kumar and H. J. R. A. Panda, *RSC Adv.*, 2015, **5**, 25676–25683.
45 I. Ahmad, S. Shukrullah, H. Hussain, M. Y. Naz, M. Irfan, O. Alyahyawy and M. Al Thagafi, *ACS Omega*, 2023, **8**, 26065–26078.
46 Z. Yan, W. Wang, L. Du, J. Zhu, D. L. Phillips and J. Xu, *Appl. Catal., B*, 2020, **275**, 119151.
47 W. Zhang, C. Xu, E. Liu, J. Fan and X. J. A. S. S. Hu, *Appl. Surf. Sci.*, 2020, **515**, 146039.
48 X. Wang, X. Wang, J. Huang, S. Li, A. Meng and Z. J. N. C. Li, *Nat. Commun.*, 2021, **12**, 4112.
49 A. Meng, W. Tian, H. Yang, X. Wang, X. Wang and Z. Li, *J. Hazard. Mater.*, 2021, **413**, 125400.
50 L. Fan, S. Lei, H. M. K. Sari, L. Zhong, A. Kakimov, J. Wang, J. Chen, D. Liu, L. Huang and J. Hu, *Nano Energy*, 2020, **78**, 105235.
51 Z. Jin, Y. Li and Q. Ma, *Trans. Tianjin Univ.*, 2021, **27**, 127–138.

52 Y.-J. Chen, M.-H. Li, J.-C.-A. Huang and P. Chen, *Sci. Rep.*, 2018, **8**, 7646.
53 C. Maheu, L. Cardenas, E. Puzenat, P. Afanasiev and C. J. P. C. C. P. Geantet, *Phys. Chem. Chem. Phys.*, 2018, **20**, 25629–25637.
54 A. Šutka, F.-K. Shieh, M. Kinka, L. Lapčinskis, C.-C. Chang, P. K. Lam, K. Pudzs and O. Verners, *RSC Adv.*, 2023, **13**, 41–46.
55 W. Li, J.-J. Li, Z.-F. Liu, H.-Y. Ma, P.-F. Fang, R. Xiong and J.-H. Wei, *Rare Met.*, 2024, **43**, 533–542.
56 R. Jiang, D. Wu, G. Lu, Z. Yan, J. Liu, R. Zhou and M. Nkoom, *J. Taiwan Inst. Chem. Eng.*, 2019, **96**, 681–690.
57 P. Zhou, J. Yu and M. J. A. M. Jaroniec, *Adv. Mater.*, 2014, **26**, 4920–4935.
58 Q. Xu, L. Zhang, B. Cheng, J. Fan and J. Yu, *Chem*, 2020, **6**, 1543–1559.
59 F. He, A. Meng, B. Cheng, W. Ho and J. C. Yu, *Chin. J. Catal.*, 2020, **41**, 9–20.
60 J. Mu, F. Teng, H. Miao, Y. Wang and X. J. A. S. S. Hu, *Appl. Surf. Sci.*, 2020, **501**, 143974.
61 T. Hu, K. Dai, J. Zhang, G. Zhu and C. J. M. L. Liang, *Mater. Lett.*, 2019, **257**, 126740.
62 K. Filipović, M. Kostić, S. Najdanović, V. M. Radović, N. Velinov, D. Bojić and A. Bojić, *Adv. Technol.*, 2023, **12**, 75–83.
63 S. Asghar, M. Roudgar-Amoli, A. Alizadeh and Z. Shariatinia, *Water, Air, Soil Pollut.*, 2023, **234**, 43.
64 M. A. Sachit and S. H. Kareem, *Baghdad Sci. J.*, 2023, 1029.
65 N. Ahmad, F. S. Arsyad, I. Royani and A. Lesbani, *Results Chem.*, 2023, **5**, 100766.
66 B. N. S. Al-dhawi, S. R. M. Kutty, A. M. Alawag, N. M. Y. Almahbashi, F. A. H. Al-Towayti, A. Algamili, N. Aminu, A.-B. A. Al-Mekhlafi, A. H. Birniwa and A. H. Jagaba, *Case Stud. Chem. Environ. Eng.*, 2023, **8**, 100508.
67 O. P. Murphy, M. Vashishtha, P. Palanisamy and K. V. Kumar, *ACS Omega*, 2023, **8**, 17407–17430.
68 X. Yang, C. Wang, B. Zhou and S. Cheng, *J. Anal. Methods Chem.*, 2023, **2023**, 9985984.
69 D. Brahma and H. Saikia, *Inorganic and Nano-Metal Chemistry*, 2023, 1–16.
70 T. Florence, *Aust. J. Chem.*, 1965, **18**, 609–618.
71 Z. Zaheer, A.-A. Aisha and E. S. Aazam, *J. Mol. Liq.*, 2019, **283**, 287–298.
72 D. S. Miller, A. J. Bard, G. McLendon and J. Ferguson, *J. Am. Chem. Soc.*, 1981, **103**, 5336–5341.